Journal of Materials Chemistry C

ROYAL SOCIETY OF CHEMISTRY

PAPER

View Article Online
View Journal | View Issue

Cite this: J. Mater. Chem. C, 2025, 13, 8320

A zero-dimensional hybrid halide with superior water resistance for high-efficiency X-ray scintillation and solid-state lighting†

Yu-Yin Wang,[ab] Yue Wang,[a] Xin-Wei Du,[c] Xue-Hui Zhang,[a] Lin Zhao,[c] Bing-Rong Yan,[c] Ruo-Fan Zhang,[c] De-Long Liu,[a] Jing Zhang[d] and Guoming Lin *[be]

Received 23rd February 2025,
Accepted 12th March 2025

DOI: 10.1039/d5tc00788g

rsc.li/materials-c

In recent years, hybrid metal halides have gained considerable attention for optoelectronic applications due to their outstanding photophysical properties, despite challenges with stability. In this study, we present the design and synthesis of a highly stable and efficient zero-dimensional (0D) hybrid copper(I) halide, $[FBZPA]_4Cu_5Br_{13}$ (FBZPA = protonated 1-(4-fluorobenzyl)piperazine)), for advanced scintillation and solid-state lighting applications. This material exhibits efficient yellow light emission with a photoluminescence quantum yield of 88.5%, driven by radiative recombination of self-trapped excitons, which is facilitated by structural deformation and strong electron–phonon coupling within the 0D structure. $[FBZPA]_4Cu_5Br_{13}$ shows excellent scintillation properties, including a high light yield (~39 100 photons MeV^{-1}), a low detection limit (0.102 $\mu Gy_{air}\ s^{-1}$), and a high spatial resolution (15 lp mm^{-1}), making it an ideal candidate for high quality X-ray imaging. Additionally, we fabricated a white light-emitting diode (WLED) by combining $[FBZPA]_4Cu_5Br_{13}$ with a commercial blue phosphor on a UV chip. The WLED exhibited a high color rendering index of 90 with stable emission. It demonstrates remarkable stability, retaining its structure and optical properties after exposure to water, and intense light, without requiring encapsulation or chemical modifications. This study highlights $[FBZPA]_4Cu_5Br_{13}$ as a promising material for next-generation scintillation and solid-state lighting applications.

Introduction

Scintillator materials, which absorb high-energy radiation such as X-rays and gamma rays and emit light in response, are essential components in medical diagnostics, security screening, and industrial non-destructive testing.[1–4] Organic scintillators are attractive due to their low cost and ease of customization, and they can be used to fabricate large, flexible devices.[5,6] However, their primary composition of hydrocarbons leads to poor X-ray absorption, resulting in low light emission efficiency and reduced durability.[7–9] Commercial inorganic scintillators like thallium-doped cesium iodide (CsI-Tl),[10] terbium-doped gadolinium oxysulfide (Gd_2O_2S-Tb),[11] and bismuth germanate (BGO)[12] are widely used, but come with limitations such as complex preparation processes, toxicity concerns, and high costs. Recently, low-dimensional organic–inorganic hybrid halides have emerged as promising alternatives.[13–19] These materials combine the advantages of organic components, such as flexibility and customization, with the superior X-ray absorption properties of heavy metal halides. This combination has the potential to overcome the limitations of both organic and conventional scintillators.

Lead halide perovskites have garnered significant attention for their outstanding optical and electronic properties.[20–26] However, their practical application is limited due to concerns over lead toxicity and material instability. To overcome these challenges, researchers have focused on lead-free, low-dimensional metal halides for light-emitting applications. These materials show great promise, offering high photoluminescence quantum yield (PLQY), tunable optical bandgaps, large Stokes shifts and improved stability.[27–29] The combination of eco-friendliness, affordability, tunable properties, high PLQY, and strong light output positions Cu(I)-based zero-dimensional (0D) halides as promising candidates for next-generation X-ray scintillators, capable of delivering high precision and reliability in advanced imaging applications. Cu's

[a] School of Chemistry, Chemical Engineering and Materials, Jining University, Qufu, Shandong, 273155, P. R. China
[b] School of Future Membrane Technology, Fuzhou University, Fuzhou, 350108, China
[c] School of Resource & Environment and Safety Engineering, Jining University, Qufu, Shandong, 273155, P. R. China
[d] School of Physics and Chemistry, Hunan First Normal University, Changsha City, Hunan, 410205, P. R. China
[e] Department of Physics, National University of Singapore, Singapore 117551, Singapore. E-mail: lingmdbs@nus.edu.sg

† Electronic supplementary information (ESI) available. CCDC 2369729. For ESI and crystallographic data in CIF or other electronic format see DOI: https://doi.org/10.1039/d5tc00788g

abundance makes these materials affordable and suitable for large-scale production. Beyond their potential in full-color displays and solid-state lighting, lead-free metal halides have also been proven to be effective as X-ray scintillators.

Recent studies have identified copper(I)-based halides as promising eco-friendly and efficient materials for X-ray scintillation applications.[30–34] Researchers have developed various structures, including 0D and two-dimensional (2D) hybrids, which exhibit strong PL and tunable optical properties. Liu *et al.* reported broadband green emission in mononuclear Cu(I) halide complexes $(PPh_3)_2$(3-methylpyridine[CuX] (X = Cl, Br, I) for high-resolution X-ray imaging.[35] Yang *et al.* presented a 2D Cu(I) iodide hybrid (*cis*-2,6-dimethylmorpholine)$_4[Cu_4I_8]\cdot 2H_2O$, which demonstrated excellent X-ray imaging performance, high light yield, moisture resistance, and a resolution of 108 line pairs per millimeter.[36] Lian *et al.* introduced two 0D Cu(I) halide materials (tetrabutylammonium cation)CuX_2 (X = Cl, Br), emitting bright green and blue light with high efficiency, making them promising for flexible X-ray imaging due to their strong luminescence and reabsorption-free properties.[37] Wang *et al.* synthesized Cu(I) halide crystals, $(C_2H_8N)_3Cu_2I_5$ and $(C_2H_8N)_4Cu_2Br_6$, effective for X-ray imaging, capable of detecting very low radiation doses and achieving a resolution of 10 line pairs per millimeter.[38] However, despite these advantages, Cu(I)-based halides still face challenges such as low X-ray light yield, and low moisture resistance that limit their practical applications. Therefore, further research is necessary to overcome these limitations and fully realize the potential of Cu-based halide scintillators in advanced X-ray imaging technologies.

In recent years, researchers have actively explored the incorporation of fluorinated organic cations to enhance the stability of organic–inorganic hybrid materials.[39,40] Fluorinated salts have been widely utilized in functional materials due to their high thermal stability and excellent heat resistance.[17,18] Additionally, the introduction of fluorinated organic molecules has been shown to improve the water resistance and thermal stability of hybrid membranes. In this work, we synthesized a Cu(I)-based metal halide hybrid, $[FBZPA]_4Cu_5Br_{13}$ (FBZPA: protonated 1-(4-fluorobenzyl)piperazine), which exhibits a high PLQY of 88.49%, strong X-ray light yield, prolonged radiation stability, and excellent water resistance. In its structure, one $[CuBr_3]^{2-}$ triangular unit is linked to one or two $[CuBr_4]^{3-}$ tetrahedral units by their edges, forming CuBr clusters. FBZPA was selected from a wide range of commercial sources due to its desirable structural characteristics and its well-documented potential for enhancing stability in hybrid materials. These CuBr clusters are further surrounded by highly stable, hydrophobic, fluorinated aromatic nitrogen-based organic cations, contributing to the material's exceptional water resistance. The high PLQY and large Stokes shift make this halide a high-performance X-ray scintillator. Additionally, the broad excitation band and excellent water resistance make $[FBZPA]_4Cu_5Br_{13}$ highly suitable for solid-state lighting applications. This work offers a valuable platform for exploring the relationship between the structure and properties of bulk crystalline materials, advancing research and applications for 0D Cu(I) halide luminescent materials.

Results and discussion

Composition and structure

Bulk single crystals of $[FBZPA]_4Cu_5Br_{13}$ were synthesized using a solvent evaporation crystallization method, as described in the ESI.† Single-crystal X-ray diffraction analysis confirmed that $[FBZPA]_4Cu_5Br_{13}$ crystallizes in the triclinic $P\bar{1}$ space group and exhibits a 0D structure. The lattice parameters are a = 10.1218(5) Å, b = 10.2760(5) Å, c = 32.8442(16) Å, with angles α = 86.595(2)°, β = 84.229(2)°, and γ = 89.055(2)° (Fig. 1a and Table S1, ESI†). In this halide structure, Cu^+ cations are coordinated by either three or four Br^- anions, forming $[CuBr_3]^{2-}$ trigonal planar units and $[CuBr_4]^{3-}$ tetrahedral units, with Cu–Br bond lengths ranging from 2.3033(15) to 2.6347(16) Å (Fig. 1b). These triangular and tetrahedral units are edge-linked to form two types of clusters in 1 : 1 and 1 : 2 ratios, which are spatially separated by the organic $[FBZPA]^{2+}$ cations (Fig. 1c). The presence of fluorine atoms within the $[FBZPA]^{2+}$ cations enhances hydrophobicity and stability of the crystal structure. The $[FBZPA]^{2+}$ cations further create a layered structure that offers additional protection to the $[CuBr_3]^{2-}$ and $[CuBr_4]^{3-}$ clusters against oxidation and moisture-induced degradation. Powder X-ray diffraction (PXRD) analysis of the ground crystals showed a close match with the simulated pattern, indicating high purity and uniformity of the synthesized material (Fig. 1d). Elemental mapping using energy-dispersive X-ray spectroscopy (EDS) showed a uniform distribution of Cu, F, Br, C, and N throughout the crystals (Fig. 1e). Additionally, X-ray photoelectron spectroscopy (XPS) confirmed the presence of Cu in the expected +1 oxidation state, with the high-resolution Cu 3d spectrum exhibiting spin–orbit splitting peaks consistent with previously reported CuBr powder[41] (Fig. S1, ESI†).

Photoluminescence properties of $[FBZPA]_4Cu_5Br_{13}$

The $[FBZPA]_4Cu_5Br_{13}$ crystals are colorless under natural light but emit bright yellow light when exposed to a 365 nm ultraviolet (UV) lamp (Fig. 2a). When excited at 331 nm, the crystals exhibit broad-spectrum light emission centered at 564 nm, with a full width at half-maximum (FWHM) of 127 nm and a significant Stokes shift of 233 nm. The UV-vis absorption spectrum shows a sharp absorption onset, indicative of direct band-edge absorption (Fig. S2, ESI†), and a direct band gap of 3.30 eV was determined using a Tauc plot. The Commission Internationale de l'Éclairage (CIE) chromaticity coordinates of the crystals were found to be (0.43, 0.52), placing them in the yellow region of the CIE chromaticity diagram (Fig. 2b). The photoluminescence excitation (PLE) spectrum shows that $[FBZPA]_4Cu_5Br_{13}$ can be excited by UV light within the 240–380 nm range, with an optimal excitation wavelength at 331 nm (Fig. 2c). The intense luminescence of the $[FBZPA]_4Cu_5Br_{13}$ crystals is attributed to their remarkably high PLQY, reaching 88.49%. (Fig. 2d). To explore the mechanism of the broadband emission, excitation wavelength-dependent PLE spectra were analyzed. These spectra exhibited consistent shapes across emission wavelengths from 450 to 700 nm and excitation wavelengths from 270 to 370 nm, indicating that the broadband emission originates from the same excited states. This rules out the possibility of Cu^+ ion luminescence arising from different excited-state levels. PL decay times at 80 K and 300 K were measured to be 107.6 μs and

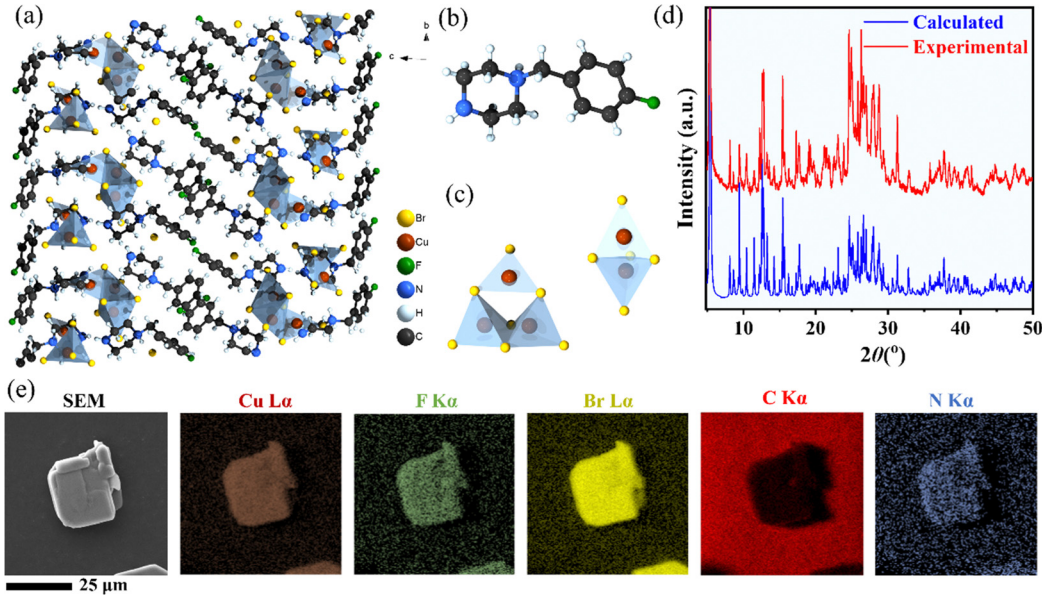

Fig. 1 Structural characterization of $[FBZPA]_4Cu_5Br_{13}$ crystals. (a) Arrangement of molecules in the crystal viewed along the *a*-axis. (b) Structural diagram ofthe $[FBZPA]^{2+}$ cation. (c) The $[Cu_3Br_7]^{4-}$ and $[Cu_2Br_5]^{3-}$ clusters. (d) Experimental and simulated PXRD patterns of $[FBZPA]_4Cu_5Br_{13}$. (e) SEM images along with the EDS elemental mapping of the synthesized microparticles.

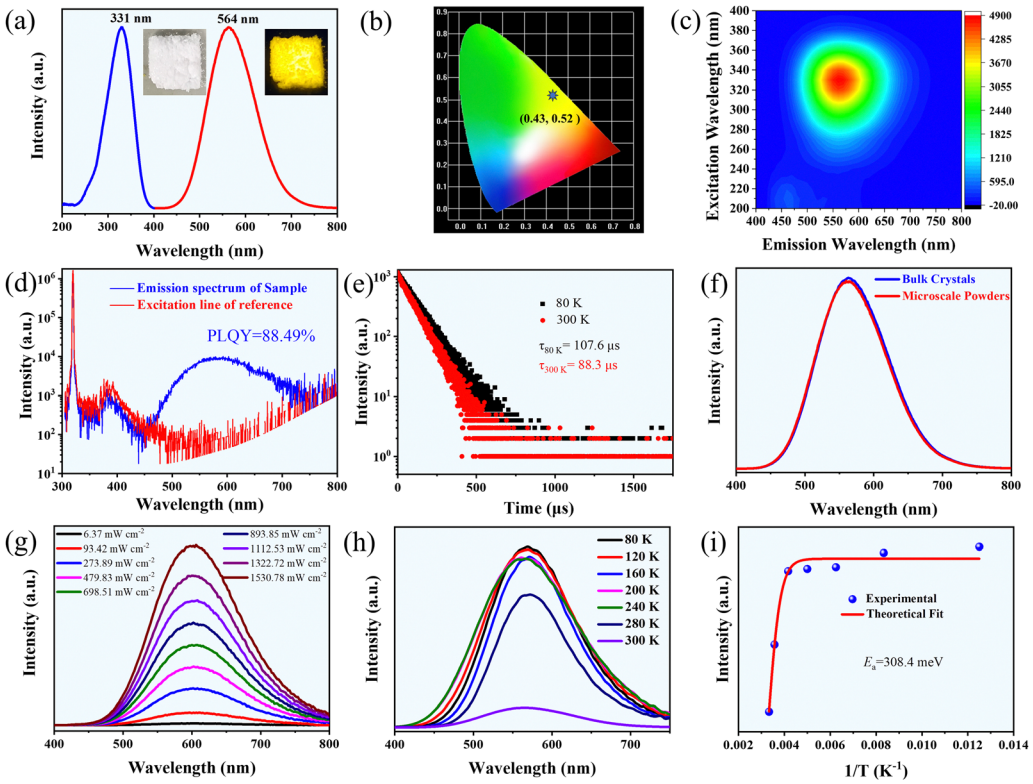

Fig. 2 PL property characterization of $[FBZPA]_4Cu_5Br_{13}$. (a) Excitation and emission spectra, with an inset image showing a photograph of the crystals excited by a 365 nm UV light. (b) CIE chromaticity coordinate image. (c) A three-dimensional color map displaying the PL emission at different excitation wavelengths. (d) PLQY of the bulk crystals. (e) PL decay curves and their fitting at temperatures of 80 and 300 K. (f) PL spectra comparison between bulk and microscale crystals. (g) PL emission intensity as a function of excitation power. (h) Emission spectra recorded over a temperature range of 80 K to 280 K. (i) Integrated PL intensity plotted against the reciprocal of temperature.

88.3 μs, respectively, suggesting that the emission involves long-lived excited states, with non-radiative decay processes increasing at higher temperatures (Fig. 2e). Bulk and micrometer-scale crystals exhibit almost identical PL suggesting that the luminescence properties of the materials are primarily determined by their intrinsic structure, despite being significantly affected by size or surface effects (Fig. 2f). The broad FWHM, prolonged lifetime, and significant Stokes shift suggest that the broadband emission originates from the radiative recombination of self-trapped excitons (STEs), a behavior commonly observed in various 0D hybrid metal halide structures. This claim is further supported by the linear relationship between excitation power density and emission intensity (Fig. 2g). To further explore the PL mechanism, a temperature-dependent PL emission spectroscopy study was conducted across a range of 80 K to 300 K (Fig. 2h). A slight variation in emission wavelength with temperature is likely attributed to minor shifts in the bandgap and thermal expansion effects, both of which minimally affect the overall emission characteristics. Additionally, the emission intensity consistently increased as the temperature decreased from 300 K to 80 K, indicating a reduction in thermal quenching and non-radiative recombination processes. The temperature-dependent emission behavior is influenced by electron–phonon coupling, which can cause an enhancement of the emission at lower temperatures by suppressing non-radiative pathways.

The thermal activation energy (E_a) was determined by fitting the integrated emission intensity as a function of temperature using the Arrhenius equation:

$$I_{PL} = \frac{I_0}{1 + A\exp\left(-\frac{E_a}{k_B T}\right)} \quad (1)$$

where I_{PL} represents the integrated emission intensity at temperature T, I_0 is the integrated emission intensity at 0 K, A is a constant, and k_B is the Boltzmann constant. The calculated E_a value was 308.4 meV, which is significantly higher than the thermal dissociation energy for free excitons at 300 K (26 meV) (Fig. 2i).[29,30] This result indicates the formation of stable bound excitons within the $[FBZPA]_4Cu_5Br_{13}$ crystals. Furthermore, as the temperature increased, the emission spectrum broadened due to enhanced electron–phonon coupling effects. Consequently, the high PLQY observed in $[FBZPA]_4Cu_5Br_{13}$ can be primarily attributed to its unique 0D structure, which provides strong quantum confinement and reduces non-radiative recombination, thereby enhancing PL efficiency.

Radioluminescence properties of $[FBZPA]_4Cu_5Br_{13}$

The scintillation properties of the synthesized $[FBZPA]_4Cu_5Br_{13}$ single crystals were thoroughly evaluated by analyzing factors such as steady-state scintillation yield, X-ray intensity-dependent luminescence, detection limits, and X-ray imaging. Under X-ray excitation, the optically transparent bulk crystals exhibited a yellow emission (Fig. 3a). The steady-state scintillation light yield of $[FBZPA]_4Cu_5Br_{13}$ was determined by comparing the integrated radioluminescence (RL) intensity with that of LuAG:Ce, a reference scintillator with a known light yield of 25 000 photons MeV^{-1}. Both samples were prepared with equal thicknesses of 3 mm and identical surface areas to ensure an accurate comparison. The light yield for the $[FBZPA]_4Cu_5Br_{13}$ sample was then calculated using the following formula:

$$\text{Light yield}_{\text{sample}} = 25\,000 \times \left(\frac{\text{RL integral area}_{\text{sample}}}{\text{RL integral area}_{\text{LuAG:Ce}}}\right) \quad (2)$$

A scintillation yield of approximately 39 100 photons MeV^{-1} was obtained for $[FBZPA]_4Cu_5Br_{13}$. The RL emission peak closely aligned with the PL emission, suggesting minimal contribution

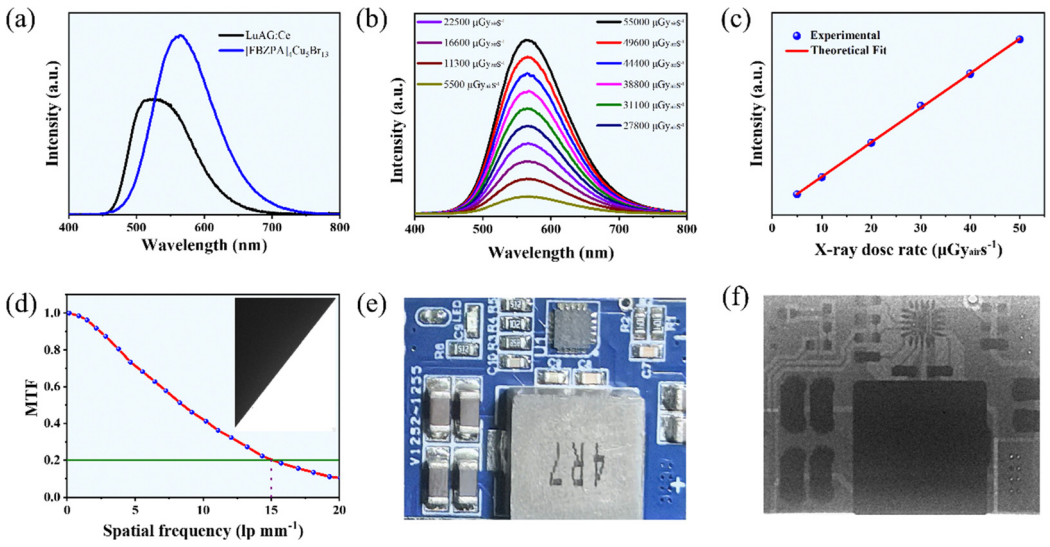

Fig. 3 Scintillation performance of $[FBZPA]_4Cu_5Br_{13}$ crystals. (a) RL spectra of $[FBZPA]_4Cu_5Br_{13}$ and LuAG:Ce under the X-ray excitation. (b) RL emission intensity of $[FBZPA]_4Cu_5Br_{13}$ as a function of X-ray dose rate. (c) The relationship between the low X-ray dose rate and RL emission intensity. (d) Modulation transfer function curve for $[FBZPA]_4Cu_5Br_{13}$ and the corresponding spatial resolution image. (e) Bright field images and (f) X-ray images of the standard X-ray resolution test conducted on a power conversion circuit board using the $[FBZPA]_4Cu_5Br_{13}$ scintillator screen.

from defect luminescence during the scintillation process. Although the calculated X-ray absorption coefficient of $[FBZPA]_4Cu_5Br_{13}$ is lower than that of LuAG:Ce (Fig. S3, ESI†), its higher RL light yield enables it to exhibit superior luminescence performance. Additionally, the RL intensity increased linearly with strong X-ray dose rates ranging from approximately 5000 to 55 000 $\mu Gy_{air}\ s^{-1}$ (Fig. 3b), demonstrating good proportionality and making it suitable for quantitative X-ray detection. X-ray dose rates were calibrated with an ion chamber dosimeter to ensure accuracy. Detection limits were established by comparing the RL spectra obtained under dark conditions with those measured at specific, controlled radiation levels. Under low X-ray dose rates, the RL intensity remains linearly correlated with the dose rates (Fig. 3c). With a signal-to-noise ratio (SNR) of 3, the detection limit for $[FBZPA]_4Cu_5Br_{13}$ was calculated to be 0.102 $\mu Gy_{air}\ s^{-1}$. Remarkably, the detection limit is just 1/55th of the threshold (5.5 $\mu Gy_{air}\ s^{-1}$) needed for X-ray medical diagnostics, highlighting its exceptional sensitivity. The spatial resolution assessment of the $[FBZPA]_4Cu_5Br_{13}$ scintillation screen revealed a resolution of 15.0 lp mm^{-1} at a modulation transfer function (MTF) of 0.2 (Fig. 3d), which is comparable to those of other metal halide-based scintillators. By positioning a power conversion module and a communication interface module circuit board in the X-ray imaging platform and utilizing $[FBZPA]_4Cu_5Br_{13}$ microparticles as a thin scintillation screen on transparent glass, we demonstrated its excellent X-ray imaging performance (Fig. 3e and f). These results highlight the potential of $[FBZPA]_4Cu_5Br_{13}$ as a scintillator for radiography and advanced imaging applications.

Photophysical mechanism of $[FBZPA]_4Cu_5Br_{13}$

To gain deeper insight into the photophysical properties of $[FBZPA]_4Cu_5Br_{13}$, density functional theory (DFT) calculations were conducted. The electronic structure analysis revealed that the material has a direct band gap, consistent with the UV-vis analysis, with both the valence band maximum (VBM) and the conduction band minimum (CBM) located at the *R*-point in the Brillouin zone. The calculated band gap is 3.14 eV, slightly lower than the experimentally measured value of 3.30 eV (Fig. 4a). The total density of state (TDOS) and partial DOS calculations indicated that the VBM is mainly composed of Cu 3d, Br 4p, and the ligand's N 2p orbitals, while the CBM is primarily comprised of Cu 4s orbitals and contributions from the organic ligand (Fig. 4b). This suggests that both the inorganic Cu–Br clusters and the organic $[FBZPA]^{2+}$ cations play a role in the electronic transitions. The charge density of the highest occupied molecular orbital (HOMO) revealed that the charge is primarily concentrated around the Br and Cu atoms as well as the ligand, whereas the charge density of the lowest unoccupied molecular orbital (LUMO) is mainly localized on the ligand (Fig. 4c and d). This charge distribution is consistent with the DOS analysis, indicating significant charge transfer between the inorganic clusters and organic cations upon excitation.

Moreover, calculations of bond lengths and bond angles in both the ground and excited states reveal significant structural changes upon excitation (Fig. 4e and f). In the excited state, the longer Cu–Br bond lengths increase, while the shorter Cu–Br

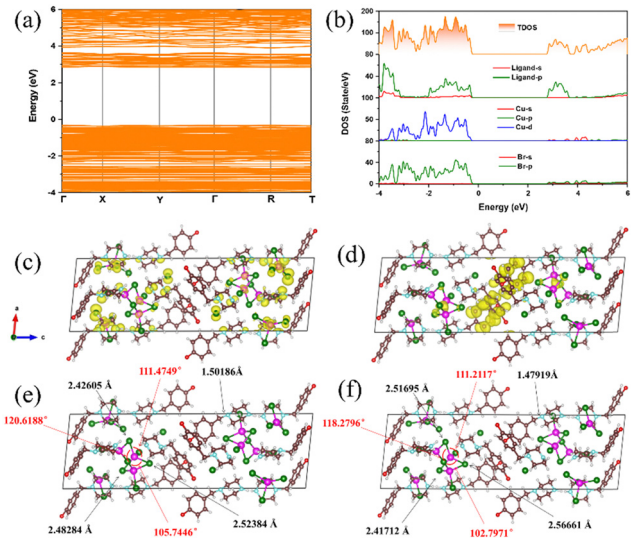

Fig. 4 Electronic structure analysis of $[FBZPA]_4Cu_5Br_{13}$. (a) The calculated electronic band structure, and (b) the calculated total density of states (TDOS) along with the partial DOS plots. (c) The calculated VBM and (d) the CBM. (e) The calculated ground state and (f) excited state.

bond lengths decrease compared to the ground state. Additionally, the C–N bridging bond in the ligand shortens upon excitation. These changes suggest that the $[CuBr_4]^{3-}$ tetrahedra undergo Jahn–Teller distortion, a phenomenon typically associated with d^9 Cu(II) complexes, but also present in Cu(I) systems due to pseudo-Jahn–Teller effects. This distortion leads to the formation of STEs, which are responsible for the observed broadband emission, characterized by a large Stokes shift and extended lifetimes. The distortion localizes the excited state, reducing non-radiative recombination and enhancing the PL efficiency. These theoretical insights align well with experimental observations, such as high PLQY, significant Stokes shift, and temperature-dependent emission properties. The interaction of structural distortion and charge transfer between the inorganic clusters and organic cations plays a crucial role in the photophysical behavior of $[FBZPA]_4Cu_5Br_{13}$, making it a promising candidate for X-ray scintillation and optoelectronic applications.

Stability properties of $[FBZPA]_4Cu_5Br_{13}$

$[FBZPA]_4Cu_5Br_{13}$ exhibits exceptional structural and spectral stability, maintaining its integrity after extended soaking in regular DI water for 20 days or subjecting to intense light irradiation (300 W Xe lamp) for 30 hours (Fig. 5a and b). Additionally, XPS analysis confirmed that Cu remains in the expected +1 oxidation state even after 20 days of water soaking (Fig. S1, ESI†). This remarkable stability is reflected in only minor shifts in emission bands, a slight reduction in PL intensity, and minimal changes in PXRD patterns (Fig. 5c and d). The exceptional water stability of $[FBZPA]_4Cu_5Br_{13}$ can be attributed to its unique structural characteristics. Specifically, the CuBr clusters are encapsulated by organic $[FBZPA]^{2+}$ cations, which not only enhance the overall structural integrity but also form hydrogen bonds that shield the Cu(I)-based core from hydrolysis. Furthermore, the hydrophobic

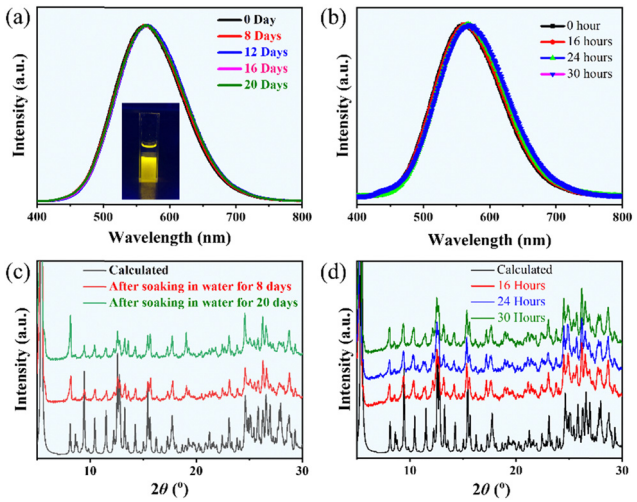

Fig. 5 Stability properties of $[FBZPA]_4Cu_5Br_{13}$ crystals. (a) PL spectra of $[FBZPA]_4Cu_5Br_{13}$ crystals soaked in water for various durations at 300 K. The inset image shows the crystals after 20 days of soaking under 365 nm UV light excitation. (b) PXRD pattern of crystals after 8 and 20 days of soaking in water. (c) PL spectra and (d) PXRD patterns of crystals exposed to high-intensity Xe light for 16, 24 and 30 hours, respectively.

nature of the fluorophenyl group in the $[FBZPA]^{2+}$ cation significantly reduces water-induced degradation by limiting moisture penetration. In summary, $[FBZPA]_4Cu_5Br_{13}$ maintains its structural and optical properties across various challenging environments, including water and intense light exposure, while consistently emitting yellow light.

Performance of the WLED

The efficient and stable luminescence of $[FBZPA]_4Cu_5Br_{13}$ prompted us to explore its potential in solid-state lighting applications. A WLED device was fabricated through coating a mixture of $[FBZPA]_4Cu_5Br_{13}$ and a commercial blue phosphor, $(BaMgAl_{10}O_{17}:Eu^{2+})$, onto a UV chip emitting at 365 nm (Fig. 6a). The resulting WLED emitted bright light with a correlated color temperature (CCT) of 6012 K, a high color rendering index (CRI) of 90, and CIE chromaticity coordinates of (0.32, 0.35), closely resembling those of natural sunlight (Fig. 6b). The CRI of this WLED significantly outperformed those of the commercially available $YAG:Ce^{3+}$-coated blue chips (CRI < 80), highlighting the superior light quality. Both the emission peaks and the overall spectral shape remained stable as the drive current increased, further confirming the robustness of the WLED device (Fig. 6c). During continuous operation at 20 mA, no notable drop in luminous efficiency was observed, demonstrating its excellent emission and thermal stability (Fig. 6d). This performance, combined with the material's stability, positions $[FBZPA]_4Cu_5Br_{13}$ as a promising candidate for advanced optoelectronic applications, including efficient and durable WLED devices.

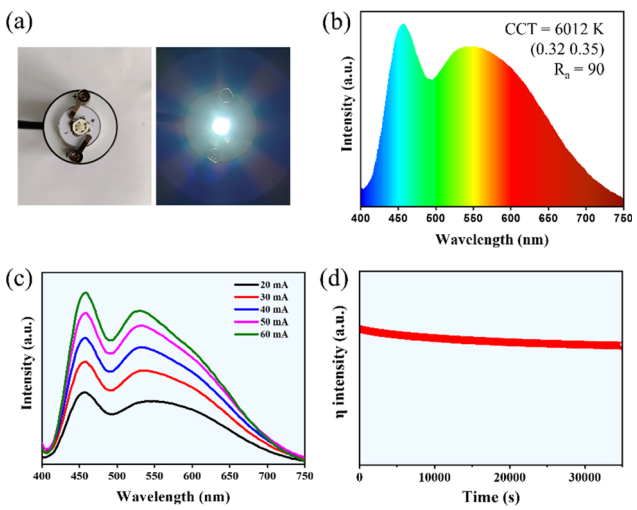

Fig. 6 Performance of the WLED using $[FBZPA]_4Cu_5Br_{13}$ crystals as a yellow-emitting phosphor. (a) Images of the fabricated white LED, including its operation at a drive current of 20 mA. (b) Electroluminescence (EL) spectrum at a drive current of 20 mA. (c) EL spectra under varying drive currents from 20 to 60 mA. (d) Time-dependent luminescence efficiency during continuous operation.

Conclusion

We successfully designed and synthesized a novel 0D hybrid Cu(I) halide, $[FBZPA]_4Cu_5Br_{13}$, which functions as a highly efficient yellow light emitter with a PLQY of 88.5%. Both experimental characterization and theoretical analysis revealed that the yellow emission results from the radiative recombination of STEs, driven by structural deformation and strong EP coupling within the 0D structure. Remarkably, $[FBZPA]_4Cu_5Br_{13}$ demonstrates exceptional chemical and physical stability under extreme conditions, including exposure to water, and intense light, without the need for encapsulation or chemical modifications. This robustness addresses the common weaknesses of organic–inorganic hybrid halides, particularly their poor water resistance. Additionally, $[FBZPA]_4Cu_5Br_{13}$ exhibits outstanding scintillation properties making it highly suitable for advanced X-ray imaging applications. Its high light yield, low detection limit, and superior spatial resolution position $[FBZPA]_4Cu_5Br_{13}$ as a strong candidate for such X-ray imaging applications. Additionally, we fabricated a WLED by combining $[FBZPA]_4Cu_5Br_{13}$ with a commercial blue phosphor on a UV chip. The resulting WLED exhibited a high CRI of 90 and CIE chromaticity coordinates close to those of natural sunlight, with stable emission under varying drive currents and continuous operation. In summary, this work opens up new possibilities for eco-friendly, water-resistant materials with excellent scintillation performance, positioning $[FBZPA]_4Cu_5Br_{13}$ as an ideal candidate for X-ray imaging and WLED applications. From the perspective of X-ray scintillation applications, iodide complexes with higher X-ray attenuation capabilities would be more suitable. Exploring such materials in future studies could be a promising direction.

Data availability

All data supporting the findings of this study are available within the manuscript and its ESI† file. Additional datasets

generated and/or analyzed during the current study are available from the corresponding author upon reasonable request.

Conflicts of interest

The authors declare no competing financial interest.

Acknowledgements

This work is financially supported by the Natural Science Foundation of China (Grant No. 22201099 and 22101282), Shandong Provincial Natural Science Foundation (Grant No. ZR2021QB204, ZR2023QB096), and Jining University 2019, 2020 "100 Outstanding Talents" support program cultivation project (2022ZYRC1). This work is also supported by University Feature Laboratory for Energy Conversion and Nanocatalysis of Shandong Province.

References

1 C. Greskovich and S. Duclos, Ceramic scintillators, *Annu. Rev. Mater. Sci.*, 1997, **27**, 69–88.
2 K. Han, K. Sakhatskyi, J. Jin, Q. Zhang, M. V. Kovalenko and Z. Xia, Seed-crystal-induced cold sintering toward metal halide transparent ceramic scintillators, *Adv. Mater.*, 2022, **34**, 2110420.
3 Y. He, I. Hadar and M. G. Kanatzidis, Detecting ionizing radiation using halide perovskite semiconductors processed through solution and alternative methods, *Nat. Photonics*, 2022, **16**, 14–26.
4 M. Nikl and A. Yoshikawa, Recent R&D trends in inorganic single-crystal scintillator materials for radiation detection, *Adv. Opt. Mater.*, 2015, **3**, 463–481.
5 T. J. Hajagos, C. Liu, N. J. Cherepy and Q. Pei, High-Z sensitized plastic scintillators: a review, *Adv. Mater.*, 2018, **30**, 1706956.
6 M. Koshimizu, Recent progress of organic scintillators, *Jpn. J. Appl. Phys.*, 2022, **62**, 010503.
7 H. Chen, M. Lin, Y. Zhu, D. Zhang, J. Chen, Q. Wei, S. Yuan, Y. Liao, F. Chen and Y. Chen, Halogen-bonding boosting the high performance X-ray imaging of organic scintillators, *Small*, 2024, **20**, 2307277.
8 X. Du, S. Zhao, L. Wang, H. Wu, F. Ye, K.-H. Xue, S. Peng, J. Xia, Z. Sang and D. Zhang, Efficient and ultrafast organic scintillators by hot exciton manipulation, *Nat. Photonics*, 2024, **18**, 162–169.
9 M. Sénoville, F. Delaunay, M. Pârlog, N. Achouri and N. Orr, Neutron-γ discrimination with organic scintillators: Intrinsic pulse shape and light yield contributions, *Nucl. Instrum. Methods Phys. Res., Sect. A*, 2020, **971**, 164080.
10 V. Nagarkar, T. Gupta, S. Miller, Y. Klugerman, M. Squillante and G. Entine, Structured CsI (Tl) scintillators for X-ray imaging applications, *IEEE Trans. Nucl. Sci.*, 1998, **45**, 492–496.
11 W. Rossner, M. Ostertag and F. Jermann, Properties and applications of gadolinium oxysulfide based ceramic scintillators, *Electrochem. Soc. Proc.*, 1999, **98**, 94–187.
12 Z. Cho and M. Farukhi, Bismuth germanate as a potential scintillation detector in positron cameras, *J. Nucl. Med.*, 1977, **18**, 840–844.
13 V. Morad, Y. Shynkarenko, S. Yakunin, A. Brumberg, R. D. Schaller and M. V. Kovalenko, Disphenoidal zero-dimensional lead, tin, and germanium halides: highly emissive singlet and triplet self-trapped excitons and X-ray scintillation, *J. Am. Chem. Soc.*, 2019, **141**, 9764–9768.
14 S. Wu, B. Zhou and D. Yan, Low-dimensional organic metal halide hybrids with excitation-dependent optical waveguides from visible to near-infrared emission, *ACS Appl. Mater. Interfaces*, 2021, **13**, 26451–26460.
15 Y. Wang, G. Lin, B. Su, X. Wang, S. Wang, Z. Cheng, D. Li, X.-W. Lei and C.-Y. Yue, Centimeter-sized lead-free iodide-based hybrid double perovskite single crystals for efficient X-ray photoresponsivity, *Dalton Trans.*, 2022, **51**, 10234–10239.
16 Y. Wang, S. Zhang, Y. Wang, J. Yan, X. Yao, M. Xu, X.-W. Lei, G. Lin and C.-Y. Yue, 0D triiodide hybrid halide perovskite for X-ray detection, *Chem. Commun.*, 2023, **59**, 9239–9242.
17 Y.-Y. Wang, Y. Feng, X.-T. Liu, L.-Y. Cao, Q.-Y. Xu, H. Qu, T. Zhao, Y. Li and G. Lin, Organic–Inorganic Hybrid Halide X-ray Scintillator with High Antiwater Stability, *Inorg. Chem.*, 2024, **63**, 16224–16232.
18 Y.-Y. Wang, G.-H. Jia, M.-R. Huo, M.-T. Cheng, X.-Y. Chen, A.-R. Chang, J. Zhang, Y.-Y. Li and G.-M. Lin, A lead-free zero-dimensional hybrid antimony halide perovskite X-ray scintillator with exceptional emission efficiency and excellent stability as a highly sensitive fluorescent probe, *Inorg. Chem. Front.*, 2024, **11**, 5034–5042.
19 Y. Y. Wang, W. T. Song, X. R. Yao, X. Y. Chen, M. T. Cheng, G. H. Jia, H. Z. Liu, X. T. Liu, H. H. Yang and C. H. Qi, A New Polar Lead-Free Hybrid Halide X-Ray Scintillator, *Adv. Opt. Mater.*, 2024, **12**, 2400190.
20 J. Han, Y. Li, P. Shen, Q. Li, Y. Liu, Y. Wei, P. Zhang and Z. Quan, Pressure-Induced Free Exciton Emission in a Quasi-Zero-Dimensional Hybrid Lead Halide, *Angew. Chem.*, 2024, **136**, e202316348.
21 L. Liu, Y. Bai, X. Zhang, Y. Shang, C. Wang, H. Wang, C. Zhu, C. Hu, J. Wu and H. Zhou, Cation diffusion guides hybrid halide perovskite crystallization during the gel stage, *Angew. Chem.*, 2020, **132**, 6035–6043.
22 Y. Liu, Y. Zhang, Z. Yang, H. Ye, J. Feng, Z. Xu, X. Zhang, R. Munir, J. Liu and P. Zuo, Multi-inch single-crystalline perovskite membrane for high-detectivity flexible photosensors, *Nat. Commun.*, 2018, **9**, 5302.
23 G. Xing, N. Mathews, S. Sun, S. S. Lim, Y. M. Lam, M. Grätzel, S. Mhaisalkar and T. C. Sum, Long-range balanced electron-and hole-transport lengths in organic-inorganic CH3NH3PbI3, *Science*, 2013, **342**, 344–347.
24 Y. Wang, C. Sun, B. Su, X. Li, X. Meng, H. Lou, Z. Cheng, Y. Wang and G. Lin, Highly efficient broadband white-light emission in two-dimensional semi-conductive hybrid lead chlorides, *Dalton Trans.*, 2022, **51**, 14930–14936.
25 G. Lin, Y. Lin, R. Cui, H. Huang, X. Guo, C. Li, J. Dong, X. Guo and B. Sun, An organic–inorganic hybrid perovskite

logic gate for better computing, *J. Mater. Chem. C*, 2015, **3**, 10793–10798.

26 G. Lin, Y. Lin, H. Huang, R. Cui, X. Guo, B. Liu, J. Dong, X. Guo and B. Sun, Novel exciton dissociation behavior in tin-lead organohalide perovskites, *Nano Energy*, 2016, **27**, 638–646.

27 J. Jin, S. Geng, K. Han, Z. Xiao and Z. Xia, Blue-Light-Excitable Red-to-Near Infrared Photoluminescence in 0D Antimony (III) Bromide Hybrids for Supplemental Lighting, *Adv. Opt. Mater.*, 2024, 2303178.

28 Z. Li, G. Song, Y. Li, L. Wang, T. Zhou, Z. Lin and R.-J. Xie, Realizing tunable white light emission in lead-free indium (III) bromine hybrid single crystals through antimony (III) cation doping, *J. Phys. Chem. Lett.*, 2020, **11**, 10164–10172.

29 F. Locardi, M. Cirignano, D. Baranov, Z. Dang, M. Prato, F. Drago, M. Ferretti, V. Pinchetti, M. Fanciulli and S. Brovelli, Colloidal synthesis of double perovskite Cs2AgInCl6 and Mn-doped Cs2AgInCl6 nanocrystals, *J. Am. Chem. Soc.*, 2018, **140**, 12989–12995.

30 J. H. Han, T. Samanta, Y. M. Park, H. J. Kim, N. S. Manikanta Viswanath, H. W. Kim, B. K. Cha, S. B. Cho and W. B. Im, Highly stable zero-dimensional lead-free metal halides for X-ray imaging, *ACS Energy Lett.*, 2022, **8**, 545–552.

31 D.-Y. Li, J.-H. Wu, X.-Y. Wang, X.-Y. Zhang, C.-Y. Yue and X.-W. Lei, Reversible triple-mode photo-and radioluminescence and nonlinear optical switching in highly efficient 0D hybrid cuprous halides, *Chem. Mater.*, 2023, **35**, 6598–6611.

32 R. Li, Y. Zhou, X. Zhang, J. Lin, J. Chen, C. Chen, X. Pan, P. Wang, R. Chen and J. Yin, In/Bi-based Direct-and Indirect-Gap Hybrid Double-Perovskite-Derived 1D Halides with Near-Unity Quantum Yield *via* Sb^{3+} Doping, *Chem. Mater.*, 2023, **35**, 9362–9369.

33 Y.-H. Liu, N.-N. Wang, M.-P. Ren, X. Yan, Y.-F. Wu, C.-Y. Yue and X.-W. Lei, Zero-dimensional hybrid cuprous halide of [BAPMA] Cu_2Br_5 as a highly efficient light emitter and an X-ray scintillator, *ACS Appl. Mater. Interfaces*, 2023, **15**, 20219–20227.

34 Y. H. Liu, X. Yan, L. Xiao, W. Jiang, Q. Liu, T. C. Liu, T. Y. Yan, C. Y. Yue and X. W. Lei, Water-Stable 0D Hybrid Manganese Halides with Adjustable Crystal Structure and Emission Color, *Adv. Opt. Mater.*, 2023, **11**, 2301010.

35 X. Liu, Y. Jiang, F. Li, X. Xu, R. Li, W. Zhu, J. Ni, C. Ding, S. Liu and Q. Zhao, Thermally activated delayed fluorescent scintillators based on mononuclear copper(I) halide complexes for high-resolution X-ray imaging, *Adv. Opt. Mater.*, 2023, **11**, 2202169.

36 H.-J. Yang, W. Xiang, X. Zhang, J.-Y. Wang, L.-J. Xu and Z.-N. Chen, High spatial resolution X-ray scintillators based on a 2D copper(I) iodide hybrid, *J. Mater. Chem. C*, 2024, **12**, 438–442.

37 L. Lian, X. Wang, P. Zhang, J. Zhu, X. Zhang, J. Gao, S. Wang, G. Liang, D. Zhang and L. Gao, Highly luminescent zero-dimensional organic copper halides for X-ray scintillation, *J. Phys. Chem. Lett.*, 2021, **12**, 6919–6926.

38 Z. Wang, Y. Du, C. Wang, L. Ma, C. Li, T. Lin, J. Xiao and Z. Yan, Dimethylamine Copper(I) Halide Single Crystals: Structure, Physical Properties, and Scintillation Performance, *Inorg. Chem.*, 2024, **63**, 13546–13557.

39 X. Wang, K. Rakstys, K. Jack, H. Jin, J. Lai, H. Li, C. S. K. Ranasinghe, J. Saghaei, G. Zhang, P. L. Burn, I. R. Gentle and P. E. Shaw, Engineering fluorinated-cation containing inverted perovskite solar cells with an efficiency of $>21\%$ and improved stability towards humidity, *Nat. Commun.*, 2021, **12**, 52.

40 B. Kim and S. I. Seok, Molecular aspects of organic cations affecting the humidity stability of perovskites, *Energy Environ. Sci.*, 2020, **13**, 805–820.

41 R. P. Vasquez, CuBr by XPS, *Surf. Sci. Spectra*, 1993, **2**, 144–148.